JPE 15-6-24

http://dx.doi.org/10.6113/JPE.2015.15.6.1640
ISSN(Print): 1598-2092 / ISSN(Online): 2093-4718

Integrated Model of Power Electronics, Electric Motor, and Gearbox for a Light EV

Isabelle Hofman[*,**], Peter Sergeant[*,**], Alex Van den Bossche[**], Selim Koroglu[†], and Selami Kesler[***]

[*]Department of Industrial Technology & Construction, Ghent University, Gent, Belgium
[**]Dept. Electrical Energy, Systems & Automation, Electrical Energy Lab., Ghent University, Gent, Belgium
[†,***]Department of Electrical and Electronics Engineering, Pamukkale University, Denizli, Turkey

Abstract

This study presents a model of a drivetrain for an integrated design of a light electric vehicle (EV). For the drivetrain of each front wheel of the single-person, battery-powered EV tricycle consists of a battery, an inverter, and an outer rotor permanent magnet synchronous motor (PMSM), which is connected to an in-wheel gearbox. The efficiency of the inverter, motor, and gearbox is analyzed over the New European Driving Cycle. To calculate the losses and efficiency of the PMSM, the power electronics in the inverter and gearbox are used. The analytical models provide a fast, but less accurate result, useful for optimization purposes. To accurately predict the efficiency of the PMSM, a finite element model is used. The models are validated by test setups. Correspondingly, a good agreement between the measurements and the calculated results is achieved. A parameter study is performed to investigate the influence of the detailed component parameters (i.e., outer rotor radius, gear ratio, and number of pole pairs and stator slots) on the average efficiency of the drivetrain.

Key words: Electric vehicle, Finite Element Model, Permanent magnet synchronous motor

I. INTRODUCTION

With the increasing consumption of fossil fuel and the environmental effects of vehicles equipped with an internal combustion engine, the need for vehicles powered by electrical energy has drawn considerable interest. However, today's electric vehicles (EVs) are costly and have high mass energy storage. These conditions often lead to a high initial cost of the EV and to a limited driving range. Apart from the involved cost and additional mass, increasing the driving range also causes a long charging time in case of residential charging infrastructure [1] and [2].

In this study, we focus on modeling the drivetrain of a light battery-powered EV. This single-person tricycle, which consists of two front wheels and one rear wheel, is designed for commuting purposes in the city and suburbs. This EV is expected to cover a driving range of approximately 100 km and has a maximum speed of nearly 70 km/h. With its highly efficient drivetrain, the vehicle requires less batteries. Furthermore, the EV implements regenerative braking, which can increase its driving range, especially in urban regions. The drivetrain of each front wheel consists of an inverter, a motor, and a gearbox.

Regarding the motor, an outer rotor permanent magnet synchronous motor (PMSM) with concentrated windings and brushless DC (BLDC) control is applied in the drivetrain of the EV. In the literature, these motors are often preferred for traction applications because of their high energy efficiency, high torque density, and high reliability. In [3], three different motor drives for electric traction were compared with regard to their energy consumption over the New European Driving Cycle (NEDC). These motor drives were induction motor (IM), interior PM (IPM), and surface PM (SPM) with the same outer dimensions (i.e., stack diameter and stack length), the same number of pole pairs, and the same inverter size (i.e., maximum peak voltage and current). The efficiency of each motor was evaluated over the NEDC. The efficiencies of the SPM and IPM in the ECE-15 (urban cycle) area were comparable and both higher than that of the IM. In the area of

Manuscript received Mar. 9, 2015; accepted May 17, 2015
Recommended for publication by Associate Editor Sang-Won Yoon.
[†]CorrespondingAuthor: skoroglu@pau.edu.tr
Tel: +90-258-296-3063,Fax: +90-258-296-3262
[*]Dept. of Industrial Tech. & Construction, Ghent University, Belgium
[**]Dept. of Electrical Energy, Syst. & Autom., Electrical Energy Lab., Ghent University, Belgium
[***]Dept. of Electrical & Electronics Eng., Pamukkale University, Turkey

the extra-urban cycle, the efficiency of the IPM was higher than those of the IM and SPM. The efficiency of the SPM dropped significantly in the extra-urban cycle because of speed-related losses. The SPM motor losses could be limited by the axial and radial segmentations of the magnets [3]. In [4], an IPM and SPM machine with fractional slot concentrated windings were compared for a hybrid traction application. These 10-pole 12-slot machines were compared in terms of their electrical efficiency under rated-load conditions. Reddy et al. [4] concluded that none of the machines exhibit excellent performance in terms of efficiency. The motors achieve similar efficiency in spite of the difference in their loss components. In particular, the SPM machine has high losses in the magnets, whereas the PMs in the IPM machine are shielded by the rotor iron, which causes additional iron losses. Therefore, both arrangements of PMs are useful in an EV application [3]. Surface magnets are a good choice for applications with a fast dynamic response and high overload torque requirement [5].

Pulse width modulation (PWM) inverter is generally used to drive motors. The usage of this inverter influences the system power loss and the overall efficiency of a drivetrain. In [6], the additional losses in magnets and the stator iron of a PMSM were studied as function of the PWM frequency. For the considered 3 kW PMSM with surface magnets, the PWM supply increased the stator iron loss and eddy-current loss in the magnets by 26% and 69%, respectively, at the lowest considered PWM frequency of 5 kHz. The spectacular increase in magnet loss could be reduced to 15% by either segmenting the magnet or by increasing the PWM frequency to 20 kHz. An analytical model for computing magnet loss was presented in [7]. This model was used to quantify the effectiveness in circumferentially segmenting the magnets to reduce the eddy-current loss in a three-phase 42-pole 36 slot machine. The results showed that the magnet segments per pole arc significantly reduced the eddy-current loss by increasing the number of segments per pole arc (i.e., from 1 per unit to 0.1 per unit eddy-current loss when the number of magnet segments per pole arc was increased from one to four). The major effect on eddy-current reduction was obtained from two to four segments per pole. The losses due to PWM should be included in drivetrain models to accurately obtain the efficiency. Computationally efficient 3D numerical models (e.g., the method presented in [8]) can be used to compute magnet loss. The model in [8] consists of a 2D time-stepping finite element model (FEM) and a 3D magnetostatic FEM. The skin depth at the frequencies of interest is greater than both the radial dimensions and pole arc width of magnets.

In this study, a lithium polymer (LiPo) battery is used. LiPo batteries have high energy density, compact size, and good high temperature performance. According to [9], a lithium-based battery is the best candidate for light EVs (LEVs) because of its high specific power (>250 W/kg), high specific energy (>100 Wh/kg), and long battery life (>1000 cycles).

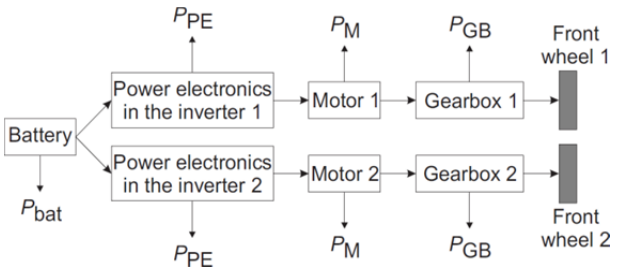

Fig. 1. Schematic overview of the complete drivetrain and power flows.

With regard to the gearbox, single- and two-stage analytical models are implemented based on the calculations described in [10]. The gearbox model is valid for all single- and two-stage spur gear gearboxes.

The parameterized component models of the electric motor as well as the power electronics (PEs) in the inverter and gearbox are presented. Each model accurately computes the efficiency as function of vehicle speed and torque. The component models are then combined into an integrated model of the drivetrain. This study aims to investigate the influence of the detailed component parameters (i.e., the outer rotor radius, number of rotor poles and stator slots of the motor, and the gear ratio of the gearbox) on the total drivetrain efficiency in reference to NEDC [11].

II. Drivetrain Modeling

Fig. 1 shows the schematic overview of each front wheel for the drivetrain model. The PEs in the inverter are supplied by a battery with a DC voltage V_{DC} and loss P_{bat}. In this paper, the term "inverter" refers to both controllers, which collectively produce the gate driver signals and PEs. In the power flow diagram of Fig. 1, the control parts of both inverters are not shown. P_{PE} is the loss of the PEs from each inverter. Each of the PMSMs, denoted by Motors 1 and 2, has a loss denoted by PM. The rotor position of the BLDC-controlled PMSM is determined by Hall sensors. These sensors are placed outside the machine and use the magnetic stray field of the outer rotor PMSM for position detection. [12] posited that this technique works well for BLDC control, and it has several advantages. The signal from the Hall sensors is sent to a complex programmable logic device (CPLD), and a three-phase motor control is achieved. The signal from the CPLD is then sent to the power stage to switch on the correct transistors to drive the motor. Finally, each of the gearboxes has a loss denoted by P_{GB}.

The structure of the drivetrain model for analyzing the efficiency is shown in Fig. 2. The input parameters of this model are the number of pole pairs (N_p), the number of stator slots (N_s), the outer rotor radius of the motor (r_{rotor}), and the

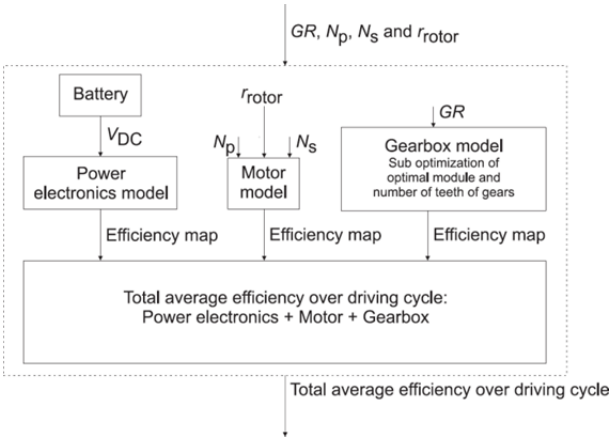

Fig. 2. Structure of the drivetrain model for analyzing efficiency.

gear ratio (GR). The output parameter is the total average efficiency over a driving cycle of the complete drivetrain.

This model contains three component models (i.e., the analytical models of the PEs in the inverter, motor, and gearbox). Each of the analytical models is discussed in Section III. Two designs of a gearbox (i.e., single- and two-stage gearbox) are implemented. Determining the module and the number of teeth of the spur gears is an optimization problem, which is shown in the drivetrain model of Fig. 2 and is evaluated for different GRs.

Section IV presents the experimental validation of all the analytical models, and Section V discusses and validates the motor model that can also be a FEM.

III. Analytical Models

In the subsequent sections, each component model (i.e., PE, motor, and gearbox models) is explained. To examine the complete drivetrain, the component models are validated and discussed in Section IV.

A. PE Model

The analytical model for PE calculates the loss P_{PE} shown in Fig. 1. This model consists of the power loss in the DC link between the battery and inverter (P_{wDC}), the switching loss (P_s) and conducting loss ($P_{rds,on}$) of the MOSFETs on the printed circuit board, the power loss in the printed wires (P_{prw}), and the copper loss in the cables between the inverter and motor (P_w). All these loss terms are included for generality of the model, but some components may be negligibly small.

The power loss in the battery (P_{bat}) is based on the instantaneous current of two motors and on its internal resistance, which is 0.109 Ω for the considered battery of 20 Ah. The loss terms P_{wDC}, P_{prw}, and P_w are Joule losses that are easily computed through the resistance of the printed wires and cables. The switching loss (P_s) is computed as

$$P_S = k \cdot V_{DC} \cdot Q_{rr} \cdot \left(\frac{I_{rms}}{I_F} \right)^{0.5} \cdot f_S \quad (1)$$

where k is a factor equal to 3 that considers the load current during commutation, and Q_{rr} is the reverse recovery charge of the intrinsic diode of the MOSFET. k can be obtained with the following equation:

$$k = \frac{E_{on}}{V_{dd} \cdot Q_{rr}} > 1 \quad (2)$$

The preceding expression describes the total amount of energy loss based on the turn-on energy E_{on} as well as the Q_{rr} charge multiplied by the DC link voltage V_{dd}. The recovery contains several conditions. When the current in the transistor is lower than the load current, the diode current remains positive. During the reverse current in the diode, the load current still adds to the diode current toward the transistor. Some parts of the losses are in the diode, whereas others are in the transistor. k increases when a low di/dt is used, but decreases if tested at a low load current to get to unity when no load current is present. A good designer often tries to achieve a compromise between a low k by fast switching and a not extremely low k for EMC reasons. In this reference, k can vary between 1.7 and 6.5 at quite a high current, but is low at a low load. According to the datasheet of the MOSFET, Q_{rr} is equal to $3.5 \cdot 10^{-6}$ Coulomb at 25 °C. However, Q_{rr} is temperature dependent. Therefore, we fit Q_{rr} with our measurements, which result in a factor of 2.25 higher than the data provided in the datasheet. This case implies that Q_{rr} is equal to $7.875 \cdot 10^{-6}$ Coulomb. The DC bus voltage (V_{DC}) is 90 V. I_{rms} is the rms value of the current waveform of the MOSFET, I_F is the forward current of the diode (I_F = 25 A from the datasheet), and f_s is the switching frequency of the MOSFETs.

The switching frequency f_s [Hz] of the MOSFETs decreases linearly with an increasing motor speed. This occurrence is caused by the fact that a constant off-time PWM algorithm is implemented. The switching frequency is calculated as follow:

$$f_S = \frac{V_{DC} - \frac{E_n \cdot f}{f_n}}{t_{OFF} \cdot V_{DC}} \quad (3)$$

where E_n is the electro motive force (EMF) at nominal speed, f is the motor frequency at a certain speed, f_n is the electrical frequency at nominal speed, and t_{OFF} is the constant off-time of the MOSFETs. Fig. 3 shows the switching frequency as a function of the motor speed. A hysteresis control is commonly used for commutation, which sets two limits for the current (an upper and a lower limit). However, in case of low inductance (e.g., short circuits in the motor windings or extreme saturation), the switching frequency can significantly increase, damaging the hysteresis controlled inverter. The switching frequency can also become extremely high because of noise (e.g., a capacitive susceptibility to dV/dt of the current sensor when the noise is larger than the hysteresis band). To limit the switching frequency to a well-known value, a constant off-time control is used. This control sets only an upper limit for the current. With this controller, the inverter can survive a load with an exceedingly low inductance. The price to pay for the

limited switching frequency is the risk of a high current ripple. Nonetheless, the constant off-time PWM can be easily implemented with a few components [13]. Another advantage is that the highest switching frequency occurs at low speed. Therefore, the additional motor losses due to PWM are low at low speed [6], and the acoustic noise is low at low speed. At high speed, the acoustic noise of tires and aerodynamics overrules the motor noise.

The conduction loss ($P_{rds,on}$) of the MOSFETs type IXTK140N20P can be computed based on $R_{ds,on}$ of $36 \cdot 10^{-3}$ Ω at an estimated operating temperature of 110 °C and I_{rms}.

$$P_{rds,on} = 3 \cdot (I_{rms})^2 \cdot R_{ds,on} \quad (4)$$

The total power loss for the PEs in the inverter (P_{PE}) is calculated with the following equation:

$$P_{PE} = P_{wDC} + P_{prw} + P_s + P_{rds,on} + P_w \quad (5)$$

Section IV-A discusses the validation of the PE model.

B. Motor Model

The loss of the outer rotor PMSM is determined by an analytical model, which has constraints on the model parameters N_p, N_s and r_{rotor} (Table I). Moreover, this model has several fixed global design parameters V_{DC} (i.e., the required nominal power (P_n) and the nominal speed of the vehicle (v_n): 20 m/s).

The analytical model based on [14] is valid for all PMSMs with surface magnets in variable speed drives. However, this model has a few drawbacks, which are not present in the FEM of Section V.

- A saturation flux density B_{tm} of 1.65 T is used to calculate the thickness of the stator teeth and rotor yoke. The flux density in the iron is 5% to 10% higher than B_{tm} because of the stacking factor of the iron sheets.
- The losses consist only of the copper loss and stator iron loss.
- The losses in the rotor yoke, magnets, and bearings as well as the additional stator iron losses by the leakage fluxes are neglected.

In [14], the following methodology is described to determine the geometry of the machine and to calculate the efficiency of the motor. The rotor back iron thickness (t_{ry}) is attained from the maximum of the air gap flux density ($B_{a,max}$).

$$t_{ry} = \frac{w_m}{2} \cdot \frac{B_{a,\max}}{B_{tm}} \cdot \frac{L_s}{L_s + L_{se}} \quad (6)$$

where w_m is the magnet width, B_{tm} is the yoke saturation flux density, L_s is the stack length (fixed at 0.04 m), and L_{se} is the additional axial length available for the rotor flux to guarantee the structural integrity of the rotor.

The model uses the star of slots theory to determine how the several concentrated stator windings can be assigned to three phases. The EMF per phase at nominal speed is based on the EMF of one side of a turn (E_t) and neglecting harmonics in the EMF.

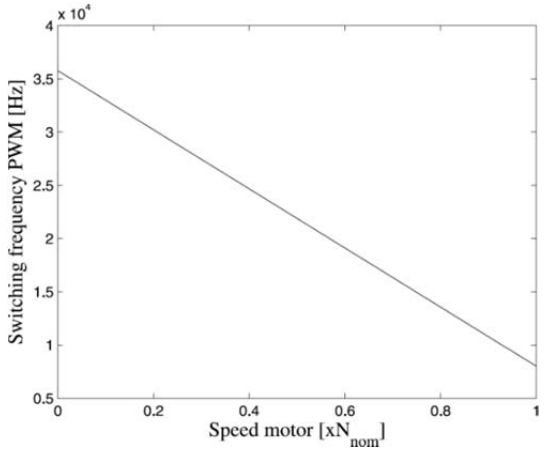

Fig. 3. Switching frequency of the MOSFETs.

TABLE I
EXPERIMENTAL AND STUDIED PMSM

Property	Symb.	Experimental PMSM	Studied PMSM
General			
Nominal speed	N_n	4500 rpm	Variable
DC bus voltage		90 V	90 V
Nominal power	P_n	1.5 kW	1.5 kW
Stator			
Outer radius	r_{so}	34.2 mm	Variable
Copper fill factor		0.3	0.3
Tooth width	w_{toth}	3.9 mm	Variable
Stack length	L_s	40 mm	40 mm
Numb. stator teeth	N_s	12	9-18
Turns per winding	N_w	10	Variable
Rotor			
Outer radius	r_{rotor}	40 mm	15120 mm
Number of pole pairs	N_p	7	3 to 8
Air gap thickness	t_a	0.55 mm	0.19 mm to 1.50 mm
Magnet-to-pole pitch ratio	α_p	0.71	0.89
Magnet radial thickness	t_m	3.55 mm	0.79 mm to 6.30 mm
Magnet width	w_m	11 mm	Variable
Magnet permeability	μ_r	1.05 μ0	1.05 μ0
Magnet remanence	B_r	1.1 T	1.1 T
Yoke saturat. flux density	B_{tm}	1.65 T	1.65 T
Addit. axial yoke length.	L_{se}	20 mm	15 mm
Iron yoke thickness	t_{ry}	1.65 mm	Variable

$$E_t = B_{a,\max} \cdot r_{so} \cdot \omega_n \cdot L_s \quad (7)$$

where r_{so} is the outer stator radius, and ω_n is the nominal mechanical speed.

The width of the stator teeth (w_{tooth}) is identified with the total flux in a tooth and the peak flux density (B_{tm}). The thickness of the tooth tips is determined in the same approach. The available space for the copper windings depends on the

tooth geometry. The number of turns is obtained by dividing the nominal voltage by the EMF per turn. The wire diameter is calculated using the fill factor, number of turns, and available space for the copper windings. The resistance per phase (R_{ph}) considers the estimated end turn length. The radial magnet thickness (t_m), the air gap thickness (t_a), the inner stator radius, and the gap width are linearly rescaled with the outer rotor radius.

The analytical model calculates the power loss of one motor (P_M).

$$P_M = P_{cu} + P_{fe} \tag{8}$$

where P_{cu} is the copper loss, and P_{fe} is the stator iron loss. The additional loss in stator iron, rotor yoke, and magnets caused by space- and time-harmonics (inclusive PWM) is neglected in the analytical model, but is considered in the FEM described in Section V. Table I illustrates the parameters of the experimental and studied PMSM. Section IV-B explains the validation of the analytical model of the motor.

C. Gearbox Model

In the gearbox model, two designs are considered (i.e., a single- and two-stage gearbox design) for a rated torque of 25 Nm. Both designs are built with parallel shafts and conventional spur gears. The single- and two-stage gearboxes are evaluated for different GRs. For the single-stage gearbox, the GRs of 1/2 to 1/7 are evaluated. Furthermore, a direct drive is evaluated without using a gearbox. For the two-stage gearbox, the GRs of 1/7 to 1/14 are evaluated.

The input parameters for the gearbox model are the rated torque, the number of teeth, and the module for the different GRs. The module of each gear pair is determined through strength calculations based on [10]. After the required module is determined, the diameter of the shafts is obtained. The output of the gearbox model is the total mass and efficiency of the gearbox. The total mass of the gearbox is the sum of the mass of the spur gears, bearings, shafts, and aluminum flanges. Section IV-C explains the efficiency of the gearbox.

The analytical model of the gearbox is general for all spur gear gearboxes in terms of the number of stages (one or two stages), module, and gear ratios (number of teeth).

1) Spur Gear Calculations: Determining the tooth bending stresses (to avoid tooth breakage) and contact stresses (to avoid pitting) is crucial on gear design. The equations for the calculation are given in [10] and can be implemented as a step by step procedure. From the calculations, the required modulus for each gear pair is obtained, and the number of teeth for each GR with the lowest mass is selected. For the single-stage gearbox, Fig. 4 shows the mass for several possible gears (motor and wheel gear combinations) for a GR of 1/2. Each of the markers defines a combination of motor and wheel gears with a different module and/or different teeth numbers. The figure clearly shows that the combination of 25 teeth at motor side and 50 teeth at wheel side with module 1 yields the lowest total mass for the different gear combinations. This approach is used for each GR and each gearbox version.

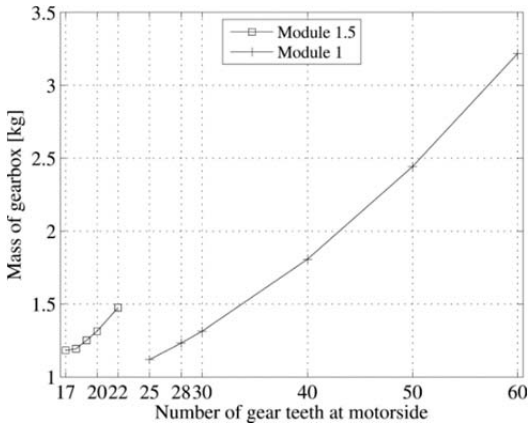

Fig. 4. Mass of the single-stage gearbox in function of the number of teeth and module for a GR of 1/2.

2) Shaft Calculations: Shear and bending moment diagrams are used to calculate the diameter of the individual shafts. The structural analysis is performed by determining the values of shear force and bending moment at each point of interest on the shaft [10]. The reaction forces on the wheel shaft are evaluated in the worst case situation (i.e., when the total load of the vehicle is distributed by only one wheel and when the driver brakes and turns at the same time). The equivalent moment of the shaft is a bending moment, which combines the acting bending moment with the torsion moment on the shaft. The final selected design diameter should be larger than the minimal diameter required to transfer the forces.

IV. Validation of the Analytical Models

The analytical models are validated through three test setups. The losses of each component can be identified separately by comparing the experimental results obtained with these test setups with the calculated results of the different component models. In each test setup, the motors are in a back-to-back configuration.

- In the first test setup, the experimental PMSM is coupled with the experimental two-stage gearbox and inverter with PWM. Table I shows the specifications of the experimental 1.5 kW PMSM with N_p: 7 and N_s: 12. For the first stage, the experimental two-stage gearbox consists of a spur gear of 18 teeth at motor side combined with a spur gear of 40 teeth on the intermediate shaft, both with a module of 1 mm. For the second stage, the two-stage gearbox is composed of a spur gear of 16 teeth at the intermediate shaft combined with a spur gear of 50 teeth at the wheel side, both with a module of 1.5 mm.
- The second test setup consists of the experimental PMSM without gearbox, but with inverter with PWM.

- In the third test setup, the experimental PMSM is coupled with an inverter without PWM. The measurements without PWM are conducted according to the mechanisms described below. The fixed DC voltage supply is replaced by a variable voltage supply. The torque set point of the controller is set to its maximum value to have no PWM. The current controller tries to realize the maximum possible current and, by consequence, the maximum possible voltage. This event results in a waveform with a consistent PWM duty cycle 1. Such a waveform is a square voltage waveform with +DC and –DC voltages as peak values. The switching frequency becomes equal to the fundamental frequency. The current and torque are controlled manually by adjusting the variable DC voltage. The electrical frequency of one PMSM varies between 50 and 600 Hz in steps of 50 Hz. The other PMSM is used as a generator to produce the load torque. The electrical power of both the motor and generator is measured by a Voltech PM6000 power analyzer.

In the following paragraphs, efficiency maps and average efficiencies are compared. The average efficiency used to validate the models is in a torque range of 0.5 T_n-T_n and in a speed range of 0.5 N_n-N_n.

A. Validation of the PE Model

The PE model is validated by comparing the measured and calculated efficiencies of the inverter with and without PWM for a motor current of 15 A (Fig. 5(a)). Both Fig. 5(a) and Table II show that the analytical model results (calculated results) correspond well to the measured results. PWM decreases the efficiency of the inverter, especially at low speed, because the switching frequency is high at low speed (Fig. 3).

The difference in comparing the average efficiency of the measured results with that of the calculated results without PWM in Table II is only 0.32%. When PWM is included in the measurements and calculations, the difference is 0.51%. Fig. 5(b) demonstrates the power loss components described in (4) for a motor current of 15 A. This figure shows that P_w , P_{prw}, and P_{wDC} are extremely small. These loss terms are included in the analytical model for the completeness of the model. Furthermore, the figure shows that in case of PWM, the switching loss P_s is dominant, and the switching loss decreases with increasing speed. This finding is again explained by the decrease of switching frequency with increasing speed as a result of the constant off-time PWM. When no PWM is used (variable DC bus voltage), the switching frequency is equal to the fundamental motor frequency, and the switching loss becomes negligible. The switching loss then increases with increasing speed because both the motor frequency and DC bus voltage increase with speed.

B. Validation of the Motor Model

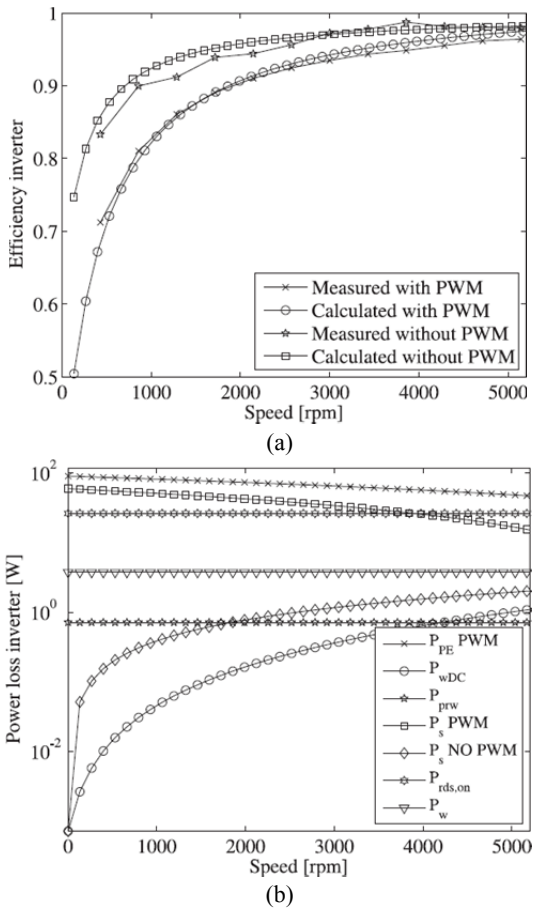

Fig. 5. Efficiency inverter at a motor current of 15 A (partial load). (a) Comparison between the measured and calculated efficiencies with and without PWM. (b) Calculated component power loss of PE in the inverter.

TABLE II
MEASURED AND CALCULATED EFFICIENCY OF THE INVERTER WITH AND WITHOUT PWM

	Inverter without PWM		**Inverter with PWM**	
	Av. eff.	Max. eff.	Av. eff.	Max. eff.
Measured	97.55%	99.77%	94.49%	99.42%
Calculated	97.87%	99.80%	95.00%	98.71%

The motor model without PWM is validated by comparing the experimental results of the third test setup without PWM with the results of the analytical model of the motor. In the analytical model of the motor in Section III-B, the additional losses in stator iron, rotor yoke, and magnets due to space- and time-harmonics (inclusive PWM) are neglected. However, these losses are considered in FEM described in Section V. Fig. 6(a) shows the measured efficiency map of the motor without PWM, and Fig. 6(b) indicates the calculated efficiency map of the motor. The efficiency map of the measured PMSM with PWM results in the efficiency map of Fig. 7. Table III illustrates the results of the efficiency of the motor with and without PWM. When the calculated results shown in Fig. 6(b) are compared with the measured results in Fig. 6(a), an average

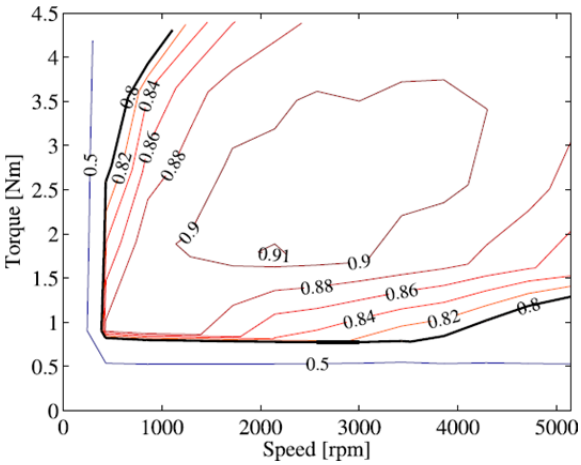

(a)

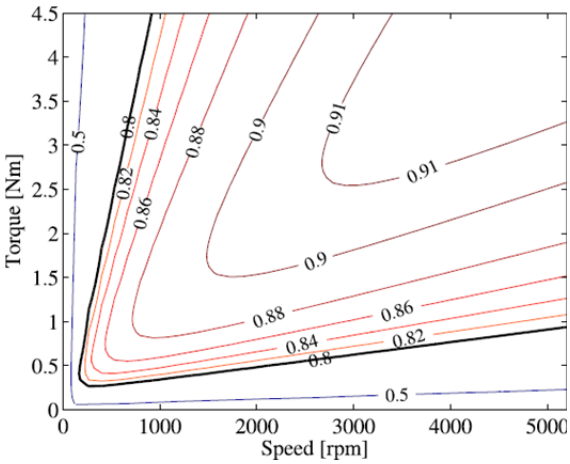

(b)

Fig. 6. Measured and calculated efficiency map of the motor without PWM; (a) measured and (b) calculated efficiency map of the motor (**analytical model**).

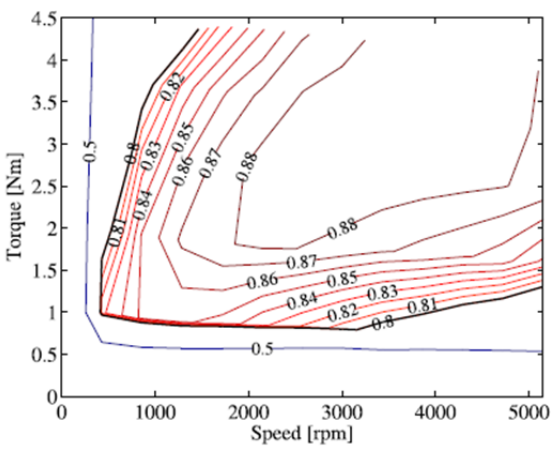

Fig. 7. Measured efficiency map of the motor with PWM.

difference of 0.90% is attained. This finding is mainly due to the drawbacks in the analytical model. The bearing, windage, and additional losses are included in the measurements, but not in the simulations. The maximum efficiency of the measured motor without PWM is reached at 2/5 of the nominal speed and 3/5 of the nominal torque. A difference of 1.92% is obtained when the average efficiencies of the measured motor with and without PWM are compared. This difference is caused by the PWM loss.

The analytical model of the motor is extremely fast, but it is not accurate enough to quantitatively predict the efficiency. Therefore a FEM of the , based on [14], is also implemented and validated by the measured results in Section V.

C. Validation of the Two-Stage Gearbox

The efficiency of the gearbox models is determined by conducting experiments on the experimental two-stage gearbox. This undertaking is performed because in the models described in the literature, the efficiency of the gearbox depends on many parameters (related to a.o. the way of lubrication and the type of oil) of which the value is hard to determine without experiments [15]. The efficiency of the single-stage gearbox (η_{1GB}) is calculated depending on the efficiency of the two-stage gearbox (η_{2GB}) with the following equation:

$$\eta_{1GB} = \sqrt{\eta_{2GB}} \tag{9}$$

An efficiency correction per stage of the gearbox with other numbers of teeth is applied based on [16].

$$\eta_{corGB} = 1 - \left(\frac{\mu}{\frac{\sin\phi}{\cos\phi}} \cdot \left(\frac{1}{z_1} + \frac{1}{z_2} \right) \right) \tag{10}$$

where μ is a fixed friction coefficient, ϕ is the pressure angle of the gear (for a conventional spur gear $\phi = 20°$), z_1 is the number of teeth of the first gear, and z_2 is the number of teeth of the second gear, which is in contact with the first gear.

The power loss of the gearbox model (P_{GB}) is determined with the measured results of the two-stage gearbox. In the first test setup, the power loss of the motor plus gearbox (P_{MGB}) can be obtained with the equation below.

$$P_{MGB} = \frac{P_{motMGB} - P_{genMGB}}{2} \tag{11}$$

where P_{motMGB} is the electrical input power of the motor, and P_{genMGB} is the electrical output power of the generator. These electrical powers are both coupled to the gearbox. In the second test setup, the power loss of the motor (P_M) can be attained with the following equation:

$$P_M = \frac{P_{mot} - P_{gen}}{2} \tag{12}$$

where P_{mot} is the electrical input power of the motor, and P_{gen} is the electrical output power of the generator. The total loss of one gearbox (P_{GB}) is expressed as:

$$P_{GB} = P_{MGB} - P_M \tag{13}$$

The model considers the number of teeth (10) for the calculation of the gearbox loss of the other gear pair combinations of a two- or single-stage gearbox. Fig. 8 depicts the resulting efficiency map of the two-stage gearbox.

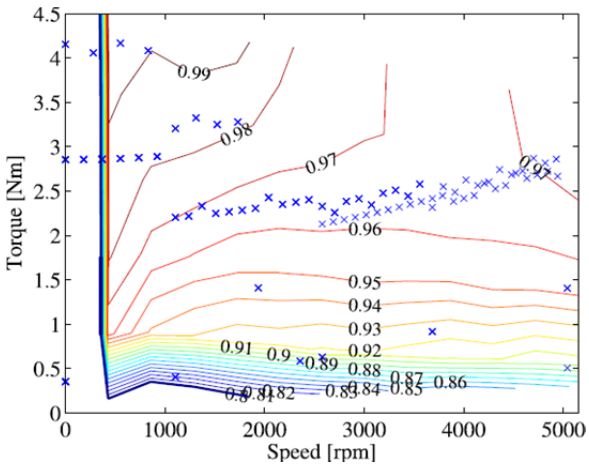

Fig. 8. Measured efficiency map of the two-stage gearbox with an average efficiency of 96.03% and a maximum efficiency of 99.51%; The crosses show the working points over the NEDC referred to the motor shaft for a GR of 1/7.

V. Finite Element Model of the Motor

The FEM of the motor, based on [14], is evaluated for a motor configuration with N_p : 7 and N_s : 12 and for a given r_{rotor} and GR. The PMSM is simulated using a sequence of static 2D FEM, varying the rotor position through the moving mesh technique. Trapezoidal current waveforms are enforced in the FEM to simulate the BLDC control of the machine. Given that a single-valued constitutive law is used, hysteresis is disregarded in FEM, but the a posteriori executed stator iron loss model considers the hysteresis losses.

The iron losses in each point of the stator depend on the time-dependent induction waveform *B(t)* and its time derivative *dB/dt*. The hysteresis, classical, and excess loss (stator iron losses) are computed for each waveform and for several load conditions. A time domain loss model is used to compute the stator iron losses, and it is based on the loss separation theory introduced in [17]. The copper loss is determined for the wire resistance computed with the analytical model and the value of the injected current.

Other than the stator iron and copper losses, the FEM also considers the additional loss terms, including the PWM loss in the stator iron $P_{fe,PWM}$, the PWM loss in the rotor $P_{rotor,PWM}$, and the magnet loss caused by the space- and time-harmonics P_{rotor}. These time-harmonics are evidently the only harmonics in the current waveform without PWM because the PWM time-harmonics are considered separately in $P_{rotor,PWM}$. Detailed information regarding the additional loss terms is given in [14].

The PWM loss is calculated with the 2D time-harmonic FEM, in which the PWM frequency (switching frequency) is applied to the stator windings. The PWM loss in the rotor is the sum of the losses for the PWM frequency and harmonics computed in both the magnets and rotor back iron. The PWM loss in the stator iron is calculated based on the stator iron losses without PWM. The additional loss caused by PWM in the stator iron is based on the following conditions:

TABLE III

Measured and Calculated Efficiencies of the Motor with and without PWM. The Analytical Model cannot Consider the PWM Loss: The Values of the Case without PWM are Repeated between Brackets

	Motor without PWM		**Motor with PWM**	
	Av. eff.	Max. eff.	Av. eff.	Max. eff.
Measured	89.48%	91.08%	87.56%	88.83%
Calculated	90.38%	91.56%	(90.38%)	(91.56%)

- The already computed hysteresis loss
- The superposition of the already computed classical losses and the additional classical losses caused by PWM
- The additional excess loss, based on [18], calculated for the PWM frequency and induction amplitude

The magnet loss caused by space-harmonics is based on the numerical method of Ede [8], which couples a 2D and 3D FEM. Flux density waveforms *B(t)* are recorded in different mesh points in the magnets (2D model) while the machine is rotating. The time derivative *dB/dt* of this flux density vector is enforced as a source term in a 3D FEM of one magnet. The 3D eddy-current problem is equivalent to a linear magnetostatic problem [8].

The total power loss of the motor calculated by the FEM ($P_{M,FEM}$) is equal to

$$P_{M,FEM} = P_{cu,FEM} + P_{fe,FEM} + P_{rotor} + P_{fe,PWM} + P_{rotor,PWM} \quad (14)$$

where $P_{cu,FEM}$ and $P_{fe,FEM}$ are the copper and stator iron losses obtained by the finite element analysis, respectively, P_{rotor} is the magnet loss caused by space-harmonics and non PWM related time-harmonics, $P_{fe,PWM}$ is the additional PWM stator iron loss, and $P_{rotor,PWM}$ is the PWM rotor loss calculated in the rotor back iron and magnets. Section VII-E describes the influence of the additional loss terms (last three terms in (14)) in FEM on the total drivetrain efficiency over a driving cycle. Parameter studies are performed to show the additional PWM loss as a function of the outer rotor radius of the PMSM and gear ratio.

A. Validation of the FEM Motor

The calculated efficiency map of the experimental motor with and without PWM, based on FEM, is shown in Figs. 9(a) and 9(b), respectively. The calculated results of FEM of the motor are shown in Table IV. The region of high efficiency in Fig. 9(b) (>80 %) is comparable with the measured results in Fig. 6(a). The same tendency is visible in Figs. 9(a) and 7. When the calculated average efficiency of FEM without PWM in Table IV is compared with the measured results without PWM, an exceedingly small difference of 0.25% is obtained. In case of the analytical model, Table III shows a difference with the measurements of 0.90%. This observation proves that FEM is more accurate than the analytical model. The comparison between the calculated results of FEM with PWM in Table IV with the measured results with PWM yields a small difference of 0.41%. Table III indicates that the result of the

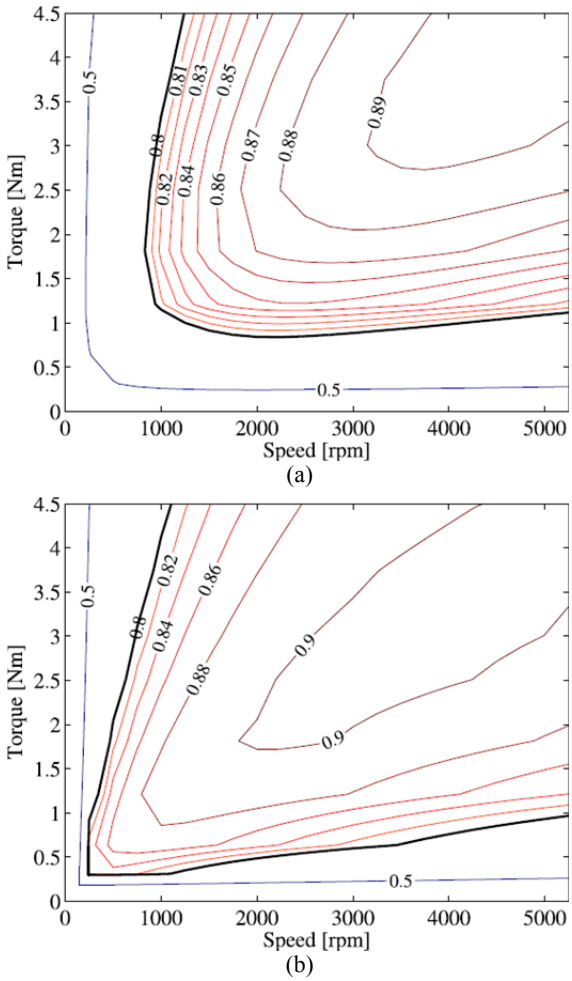

Fig. 9. Calculated efficiency map of the motor by FEM; (a) efficiency map of the motor with PWM, and (b) efficiency map of the motor without PWM.

TABLE IV
MEASURED AND CALCULATED EFFICIENCIES OF THE MOTOR BASED ON FEM WITH AND WITHOUT PWM

	Motor without PWM		Motor with PWM	
	Av. eff.	Max. eff.	Av. eff.	Max. eff.
Measured	89.48%	91.08%	87.56%	88.83%
Calcul. (FEM)	89.73%	90.41%	87.97%	89.43%

analytical model, which cannot model the PWM losses, deviates 2.41% from the measurements. For the case with PWM, FEM is more accurate than the analytical model.

VI. EFFICIENCY COMPUTATION OF DRIVETRAIN OVER THE NEW EUROPEAN DRIVING CYCLE

The efficiency of the complete drivetrain is evaluated over NEDC. The test sequence of NEDC is composed of two parts, which are an urban cycle made of four elementary ECE-15 urban cycles and an extra-urban cycle. Given that the vehicle has a maximum speed of 20 m/s, NEDC is cut off at that specific speed.

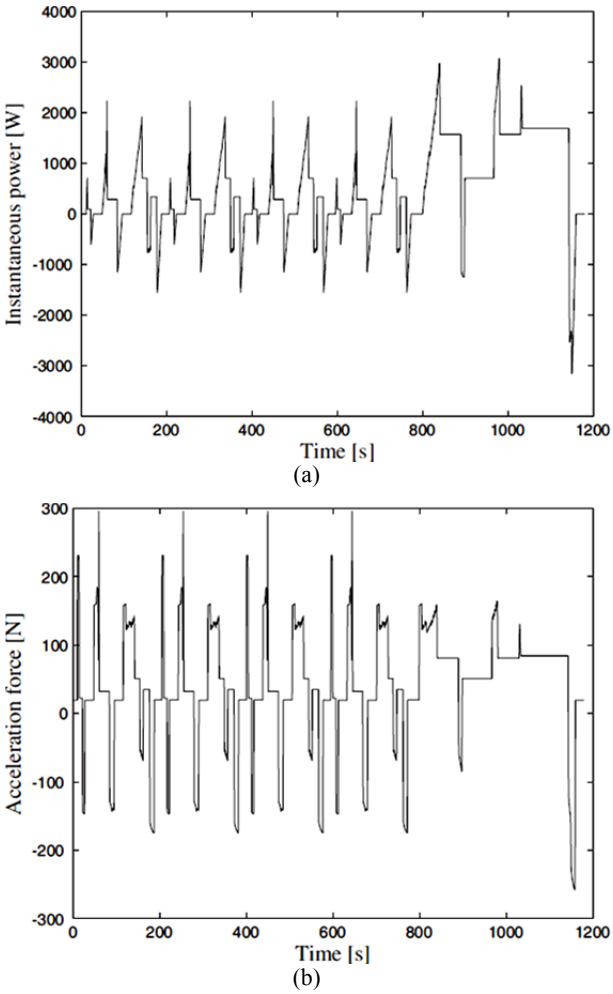

Fig. 10. Power and acceleration force for the LEV over NEDC; (a) instantaneous power and (b) acceleration force over NEDC; The theoretical energy needed to drive NEDC is 160.49 Wh. At the maximal speed of 20 m/s, the motor is at 5200 rpm.

The instantaneous acceleration force over NEDC (F_{NEDC}) is determined by the sum of the rolling force, the drag force, and the acceleration or deceleration force. The instantaneous power over NEDC (P_{NEDC}) is calculated with the below equation.

$$P_{NEDC} = F_{NEDC} \cdot v_{NEDC} \tag{15}$$

where v_{NEDC} is the instantaneous speed over NEDC. Fig. 10 illustrates the power and acceleration force required over NEDC.

The theoretical energy needed to drive NEDC (E_{NEDC}) is calculated by integrating P_{NEDC} over the NEDC time (t_{NEDC}) and is equal to 160.49 Wh. The total loss of the drivetrain (P_{DT}) (16) is the sum of the losses in the battery (P_{bat}), the losses of PE in the two inverters (P_{PE}), the losses in the two PMSMs (P_M), and the losses in the two gearboxes (P_{GB}) (Fig. 1).

$$P_{DT} = P_{bat} + (P_{PE} \cdot 2) + (P_M \cdot 2) + (P_{GB} \cdot 2) \tag{16}$$

The power loss in each working point of NEDC ($P_{DT,NEDC}$) is determined by interpolating the losses over the required speeds and torques in NEDC. The crosses in Fig. 8 show the working points over NEDC. In these points, the power loss is

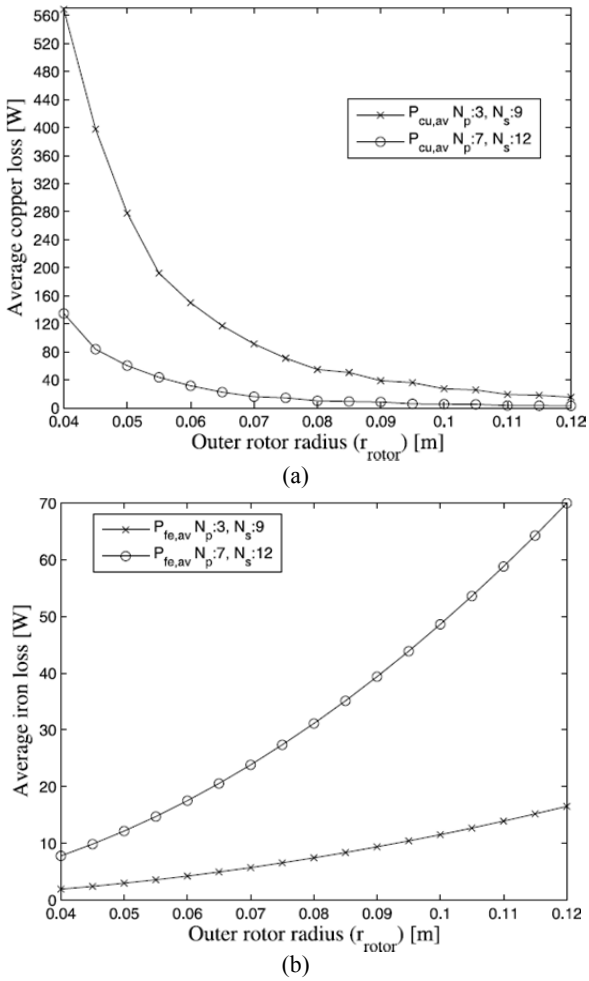

Fig. 11. Influence of the outer rotor radius on the average copper and average stator iron loss for a gear ratio of 1/4 and for two different motor configurations (N_p : 3, N_s : 9 and N_p : 7, N_s : 12) without PWM (analytical model); Influence of the outer rotor radius (a) on the average copper loss and (b) average stator iron loss.

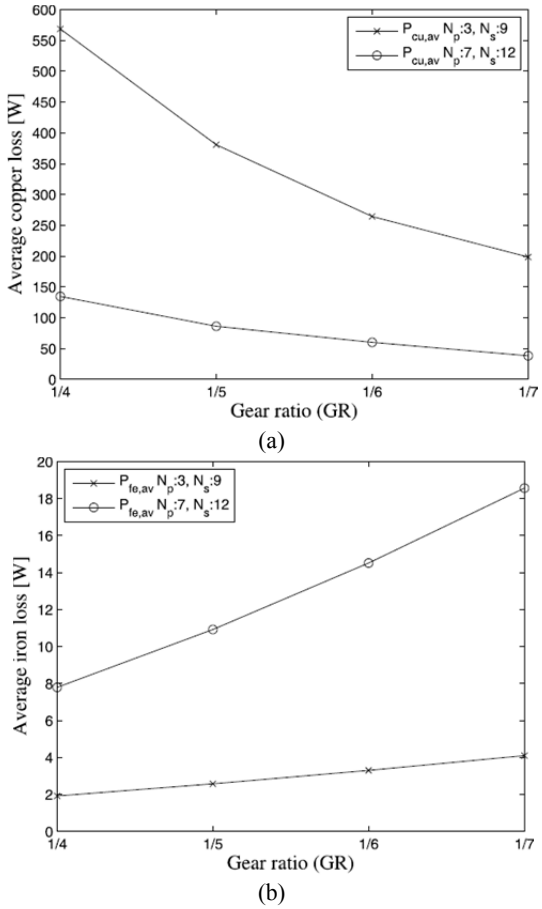

Fig. 12. Influence of gear ratio on the average copper and average stator iron loss for an outer rotor radius of 0.040 m and for two different motor configurations (N_p: 3, N_s: 9 and N_p: 7, N_s: 12) without PWM (analytical model); Influence of the gear ratio on the (a) average copper loss and (b) average stator iron loss.

determined. The total energy loss of the drivetrain over NEDC ($E_{DT,NEDC}$) is calculated by integrating $P_{DT,NEDC}$ over t_{NEDC}. The total average efficiency of the complete drivetrain ($\eta_{DT,NEDC}$) is obtained by dividing the total output energy over NEDC (E_{NEDC}) by the total input energy over NEDC (E_{NEDC}+ $E_{DT,NEDC}$).

VII. Parameter Study

A parameter study is conducted to investigate the influence of the parameters r_{rotor} , GR, N_p, and N_s on the average efficiency. The different loss terms (e.g., copper loss, stator iron loss, additional PWM loss, etc.) are shown separately to gain insights into the influence of each parameter on each loss component. For the FEM of the motor, the influence of the additional PWM loss on r_{rotor} and GR is discussed.

A. Influence of the Outer Rotor Radius

The outer rotor radius strongly influences the copper and stator iron losses of the motor (Figs. 11(a) and (b)). A large outer rotor radius increases the EMF per turn because the flux per pole increases. Given that the DC voltage is fixed, the number of turns decreases when the EMF per turn increases. As such, the wire diameter can increase. The slot surface increases as well, providing additional spaces for thick wires. By contrast, the resistance per phase is drastically reduced similar to the average copper loss ($P_{cu,av}$) (Fig. 11(a)). When the outer rotor radius increases, the total amount of iron increases, which results in an increasing average stator iron loss ($P_{fe,av}$). Moreover, Fig. 11(b) indicates that the average stator iron loss increases almost quadratically with the outer rotor radius. Therefore, a large outer rotor radius will decrease the average copper loss and increase the average stator iron loss of the motor.

B. Influence of the Gear Ratio

Increasing the gear ratio increases the nominal speed and hence the electrical frequency (f_n) of the motor. In this case, the EMF per turn increases again [see (7)]. Therefore, the number

of turns and the resistance per phase decrease. Consequently, the average copper loss ($P_{cu,av}$) decreases as shown in Fig. 12(a). In particular, the average copper loss decreases almost quadratically with the gear ratio. When the nominal electrical frequency is proportional to the gear ratio, the average stator iron loss ($P_{fe,av}$) in Fig. 12(b) increases with a power between 1.3 and 1.6 of the gear ratio, depending on the magnetic material grade. A large gear ratio has the same effect as increasing the outer rotor radius, that is, a large gear ratio decreases the average copper loss, but increases the average stator iron loss (Fig. 12).

C. Influence of the Number of Pole Pairs and Stator Slots

The influence of the number of pole pairs (N_p) and stator slots (N_s) on the average copper and average stator iron loss of the motor is investigated based on the plotted results in Figs. 11 and 12.

In this test, we first consider the influence of the number of pole pairs. The magnet width decreases as the number of pole pairs increases, which results in a thin rotor yoke. When the rotor yoke becomes thin, the outer stator radius and total flux per pole increase due to the large diameter and constant radial thickness of the air gap. The EMF per turn increases, resulting again in a low number of turns, and the slot surface slightly increases (also because of the large air gap radius). Consequently, for a high number of poles, the resistance per phase and the average copper loss ($P_{cu,av}$) decrease. Moreover, when the number of pole pairs increases, the nominal electrical frequency of the motor increases for the same nominal vehicle speed, wheel diameter, and gear ratio. Therefore, the average stator iron loss ($P_{fe,av}$) increases.

Correspondingly, we then examine the influence of the number of stator slots. Given that several slots (and teeth) exist for almost the same tooth width, the amount of iron increases, but the total copper surface reduces. This event increases the resistance per phase and the average copper loss. The increased number of slots leads to further average stator iron loss because of the huge amount of iron mass.

D. Influence of rotor radius, gear ratio, and the number of pole pairs and stator slots on the average efficiency over NEDC

The previous paragraphs discuss the influence of rotor radius, gear ratio, number of pole pairs, and stator slots on the different loss terms in the machine averaged over a torque and with a speed range of 0.5–T_n and 0.5–N_n. Therefore, we now compute the losses and efficiency over NEDC.

Fig. 13 shows the average efficiency of a complete drivetrain with a single-stage gearbox over NEDC for a fixed GR of 1/4 with four different outer rotor radii and eight different configurations of N_p and N_s.

The effects of N_p, N_s, and rotor radius are first analyzed. Given that the gear ratio is fixed, the efficiency of the gearbox over NEDC is the same for each motor configuration shown in

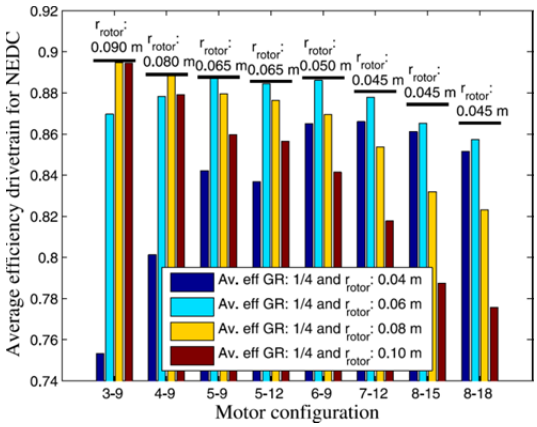

Fig. 13. Average efficiency of the drivetrain with a single-stage gearbox over NEDC for a GR of 1/4 for eight different motor configurations and four outer rotor radii; The horizontal black line denotes the maximum average efficiency for a GR of 1/4 and for each motor configuration; The motor configuration 3–9 stands for N_p: 3 and N_s: 9.

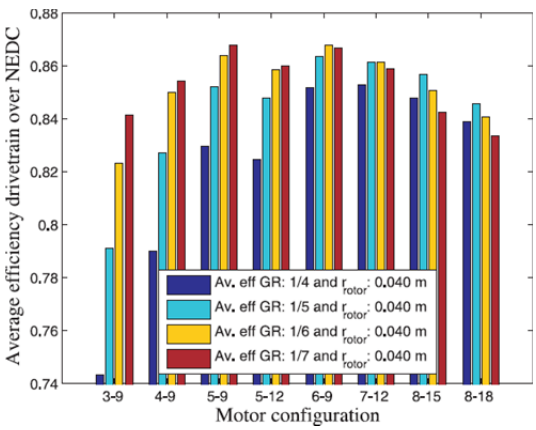

Fig. 14. Average efficiency of the drivetrain with a single-stage gearbox over NEDC for r_{rotor} of 0.04 m with four different GRs and eight different motor configurations; The motor configuration 3–9 stands for N_p: 3 and N_s: 9.

the figure. The first bar in each group of four bars, with an outer rotor radius of 0.040 m, in Fig. 13 is considered. A small outer rotor radius of 0.040 m results in a high average efficiency (85.28%) at a high number of pole pairs and stator slots (7–12). Consequently, the second bar in each group of four bars is considered. The average efficiency increases when the outer rotor radius increases to 0.060 m. Correspondingly, the highest average efficiency (87.36%) is achieved at a low N_p and N_s (5–9). Increasing the outer rotor radius to 0.080 m (bar three in each group of four bars) results in a maximum average efficiency of the drivetrain (88.07%) at low N_p and N_s (3–9) and a decreased average efficiency when N_p and N_s increase.

Therefore, a low number of pole pairs should be combined with large rotors to obtain a high efficiency. On top of the bars in Fig. 13, the "optimal" radius resulting in a high average efficiency is shown. For the lowest pole pair number, the largest rotor seems to be optimal. The balance between iron and copper loss is responsible for this observation. Increasing the rotor radius and pole pair number both decrease the copper

loss and increase the stator iron loss. For high radius and high pole pair number, the stator iron loss becomes huge and causes a low overall efficiency. An "optimal" rotor radius seems to exist for each pole pair number.

The effects of N_p, N_s, and gear ratio are then examined. In this case, the rotor radius is fixed. Fig. 14 shows the average efficiency of the complete drivetrain with a single-stage gearbox over NEDC for an r_{rotor} of 0.04 m with four different GRs and eight different configurations of N_p and N_s. The first two bars per group in Fig. 14 are considered. When the gear ratio increases, the average efficiency of the drivetrain is increased. The highest average efficiency is obtained at high N_p and N_s for low gear ratios. Increasing the gear ratio to 1/6 or 1/7 (last two bars in each group of four bars in Fig. 14) strongly increases the efficiency for low N_p and N_s, but decreases the efficiency for high N_p and N_s. The configuration with the highest efficiency is now obtained for a low N_p and N_s than for a gear ratio of 1/4.

Correspondingly, a low number of pole pairs and stator slots (i.e., 3–9 to 5–12) should be combined with high gear ratios to achieve a high efficiency. The explanation for this proposition is similar to the one in the preceding paragraph. A high pole pair number and a high gear ratio both result in low copper loss and high stator iron loss. If both N_p and GR are high, then the stator iron loss is extremely large and causes low efficiency.

E. FEM

In this section, the FEM of the machine, based on [14] and is described in Section V, is implemented in the routines to calculate the average efficiency over NEDC. The additional loss in stator iron, rotor yoke, and magnets caused by space- and time-harmonics (inclusive PWM) are added to the copper and stator iron loss, resulting in the total power loss of the motor (14).

In Fig. 15, the average efficiency over NEDC for a single-stage drivetrain is shown for different GRs and outer rotor radii for a motor configuration of N_p: 7 and N_s: 12. This figure particularly illustrates that an optimum efficiency point exists for each GR. When a high GR is selected, r_{rotor} should decrease to obtain a high average efficiency over NEDC. Increasing the GR slightly decreases the maximum average efficiency over NEDC. The tendencies are the same for the analytical model and FEM. The average efficiency of the complete drivetrain evaluated over NEDC is high when only the analytical models of the motor, PE, and gearbox are used. The analytical model underestimates the total power loss in the motor (approximately 2.46% difference) because the influence of the PWM loss is not included in the analytical model of the motor.

F. Influence of the PWM Loss

In Fig. 16, the additional rotor and stator iron loss caused by PWM is shown for a GR of 1/4 and 1/5 and with r_{rotor} of 0.045 and 0.050 m.

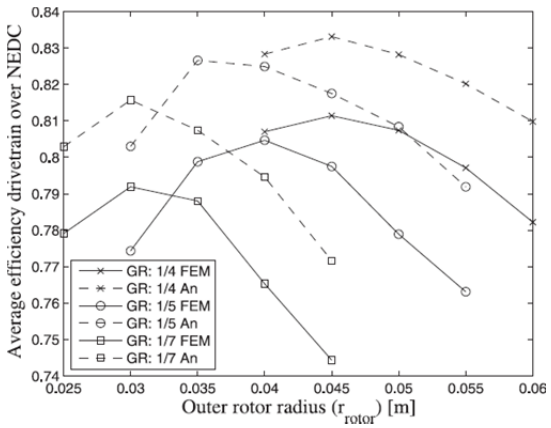

Fig. 15. Average efficiency over NEDC in function of rotor for a drivetrain with a single-stage gearbox with N_p: 7 and N_s:12.

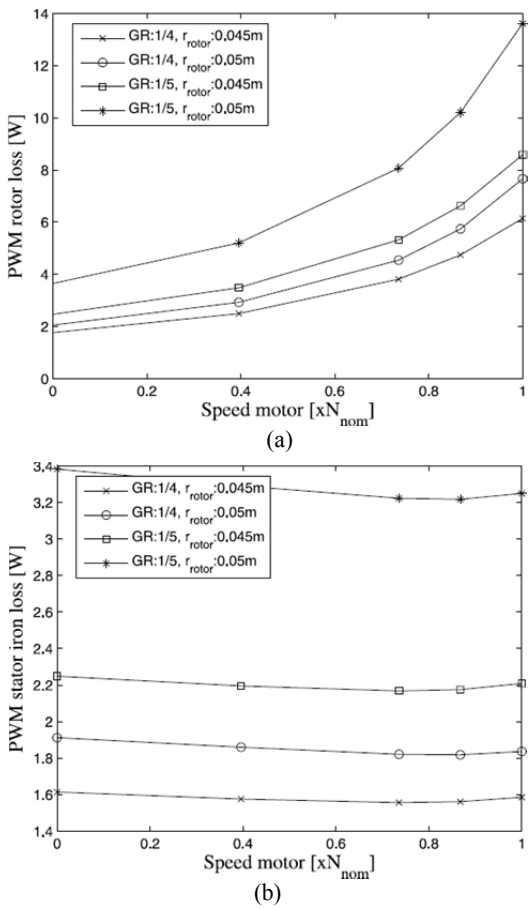

Fig. 16. Additional PWM loss in the rotor and stator iron; PWM loss in (a) the rotor (rotor back iron + magnets) and (b) stator iron.

The additional PWM rotor loss calculated in the rotor back iron and magnets increases with the speed of the motor. This occurrence is caused by the fact that the switching frequency decreases with speed. PWM loss in the motor generally increases with a low switching frequency [6]. At high switching frequency (low motor speed), the additional losses in the rotor back iron are low due to skin effect in the magnets. When the switching frequency decreases, the motor speed and the skin depth in the rotor back iron increase, causing

additional rotor losses. The additional PWM rotor loss also increases when r_{rotor} is increased. The reason behind this condition is the fact that with increasing r_{rotor}, the magnet thickness increases. However, the number of turns decreases so that the constant DC bus voltage causes large flux variations and large additional losses in thick magnets. Increasing the GR decreases the number of turns and therefore yields large flux variations and large additional losses in the magnets.

The additional PWM stator iron losses are increased by an increasing r_{rotor} because the amount of stator iron increases. Moreover, a great GR results in additional PWM stator iron losses due to the decreasing N_w, which causes large dB/dt in the motor. The additional PWM stator iron losses are almost constant over the whole motor speed.

Therefore, the additional losses in the rotor and stator iron due to PWM is not negligible compared with the losses without PWM.

VIII. CONCLUSION

Three parameterized analytical models are developed to investigate a complete drivetrain over a driving cycle. The analytical models include 1) a motor model, which is general for outer rotor permanent magnet synchronous machines, 2) a gearbox model, which is general for all spur gear gearboxes, and 3) a PE model, which considers a variable PWM frequency. The measurement results reveal that the analytical models have the same tendencies as the measured results. Therefore, the analytical models are useful for designing a good motor in combination with a gearbox, but they are not accurate enough to quantitatively predict the efficiency. Therefore, a FEM of the motor is added and validated to implement additional loss terms caused by PWM harmonics from the inverter.

Instead of presenting one optimal solution for a complete drivetrain, this study aims to provide insights into the influence of the detailed component parameters (i.e., outer rotor radius, gear ratio, number of pole pairs, and stator slots) on the total drivetrain efficiency and different loss contributions over NEDC. When the outer rotor radius is increased, the average copper loss of the motor is decreased, but the average stator iron loss is increased. The gear ratio and the number of pole pairs and stator slots similarly increase the outer rotor radius of the motor.

To attain a high efficiency over NEDC, a low number of pole pairs and stator slots should be combined with a large rotor radius and/or high gear ratios. Concerning the effect of PWM, the PWM rotor loss increases with the speed of the motor because the switching frequency decreases with increasing motor speed in the constant off-time PWM. The PWM stator iron losses are increased by an increasing outer rotor radius. Moreover, a large gear ratio results in several PWM iron losses. The additional losses in the rotor and stator iron due to PWM are not negligible compared with the losses without PWM.

ACKNOWLEDGMENT

This work was supported by the Scientific and Technological Research Council of Turkey (TUBITAK), the Fund of Scientific Research Flanders (FWO) under Grant 114E023, and the special research fund of Ghent University.

REFERENCES

[1] B.-H. Lee, D.-H. Shin, H.-S. Song, H. Heo, and H.-J. Kim, "Development of an advanced hybrid energy storage system for hybrid electric vehicles," *Journal of Power Electronics,* Vol. 9, No. 1, pp. 51-60, Jan. 2009.

[2] Y.-C. Liu, "Improvement of available battery capacity in electric vehicles," *Journal of Power Electronics,* Vol. 13, No. 3, pp.497-506, May 2013.

[3] G. Pellegrino, A. Vagati, B. Boazzo, and P. Guglielmi, "Comparison of induction and PM synchronous motor drives for EV application including design examples," *IEEE Trans. Ind. Appl.*, Vol. 48, No. 6, pp. 2322-2332, Nov./Dec. 2012.

[4] P. B. Reddy, A. M. EL-Refaie, K.-K. Huh, J. K. Tangudu, and T. M. Jahns, "Comparison of interior and surface PM machines equipped with fractional-slot concentrated windings for hybrid traction applications," *IEEE Trans. Energy Convers.,* Vol. 27, No. 3, pp. 593-602, Sep. 2012.

[5] I. Petrov and J. Pyrhonen, "Performance of low-cost permanent magnet material in PM synchronous machines," *IEEE Trans. Ind. Electron.*, Vol. 60, No. 6, pp. 2131-2138, Jun. 2013.

[6] P. Sergeant, H. Vansompel, A. Hemeida, A. Van den Bossche, and L. Dupre, "A computationally efficient method to determine iron and magnet losses in VSI-PWM fed axial flux permanent magnet synchronous machines," *IEEE Trans. Magn.*, Vol. 50, No. 8, Aug. 2014.

[7] K. Atallah, D. Howe, P. H. Mellor, and D. A. Stone, "Rotor loss in permanent-magnet brushless AC machines", *IEEE Journal of Emerging and Selected Topics in Power Electronics*, Vol. 1, pp. 3-10, 2013.

[8] J. D. Ede, K. Atallah, G. W. Jewell, J. B. Wang, and D. Howe, "Effect of axial segmentation of permanent magnets on rotor loss in modular permanent-magnet brushless machines," *IEEE Trans. Ind. Appl.*, Vol. 43, No. 5, pp. 1207-1213, Sep./Oct. 2007.

[9] A. Khaligh and L. Zhihao, "Battery, ultracapacitor, fuel cell, and hybrid energy storage systems for electric, hybrid electric, fuel cell, and plug-in hybrid electric vehicles: state of the art," *IEEE Trans. Veh. Technol.*, Vol. 59, No. 6, pp. 2806-2814, Jul. 2010.

[10] D. Muhs, H. Wittel, M. Becker, D. Jannasch, and J. Voβiek, *Uitwendige Cilindrische Tandwielen*, Roloff/Matek machine-onderdelen, 4th ed. Den Haag, Netherlands: Sdu Uitgevers, ch. 21, pp. 656-700, 2012.

[11] Regulation No 101 of the Economic Commission for Europe of the United Nations (UN/ECE), Official Journal L 138, pp. 0001-0077, 2012.

[12] P. Sergeant, A. Van den Bossche, and I. Hofman, "Magnetic stray field based position detection in BLDC outer rotor permanent magnet synchronous machines," *International Journal of Numerical Modelling: Electronic Networks, Devices and Fields*, Vol. 27, No. 3, pp. 544-554, May 2014.

[13] A. Van den Bossche, D.V. Bozalakov, T. Vyncke, and V.C. Valchev, "Programmable logic device based brushless DC

motor control," *Proceedings of the European Conference on Power Electronics and Applications*, pp. 1-10, Aug. 2011.
[14] P. Sergeant, and A. Van den Bossche, "Influence of the amount of permanent magnet material in fractional-slot permanent magnet synchronous machines," *IEEE Trans. Ind. Electron.*, Vol. 61, No. 9, pp. 4979-4989, Sep. 2014.
[15] T. T. Petry-Johnson, A. Kahraman, N. E. Anderson, and D. R. Chase, "An experimental investigation of spur gear efficiency," *Journal of Mechanical Design*, Vol. 130, No. 6, Apr. 2008.
[16] V. Ramamurti, "Efficiency of gears," in Mechanics of machines, Alpha Science International, 2010.
[17] E. Barbisio, F. Fiorillo, and C. Ragusa, "Predicting loss in magnetic steels under arbitrary induction waveform and with minor hysteresis loops," *IEEE Trans. Magn.*, Vol. 40, No. 4, pp. 1810-1819, Jul. 2004.
[18] A. M. El-Refaie, "Fractional-slot concentrated windings synchronous permanent magnet machines: opportunities and challenges," *IEEE Trans. Power Electronics*, Vol. 57, No. 1, pp. 107-121, Jan. 2010.

Isabelle Hofman received her master's degree in electromechanical engineering in 2010 from the University College of Ghent, Belgium. In 2010, she became a Ph.D. researcher in a project entitled Ecologic Low Budget Electric vehicle at Ghent University. Her research is in the field of electric drives for light electric vehicles.

Peter Sergeant received his M.Sc. degree in electromechanical engineering in 2001 and his Ph.D. degree in engineering sciences in 2006, both from Ghent University, Ghent, Belgium. In 2001, he became a researcher at the Electrical Energy Laboratory of Ghent University. After give years, he became a postdoctoral researcher at Ghent University (postdoctoral fellow of the Research Foundation - Flanders) and at Ghent University College in 2008. Since 2012, Dr. Sergeant is an associate professor at Ghent University. His current research interests include numerical methods in combination with optimization techniques to design nonlinear electromagnetic systems, in particular, electrical machines for sustainable energy applications.

Alex Van den Bossche received his M.Sc. and Ph.D. degrees in electromechanical engineering from Ghent University Belgium, in 1980 and 1990, respectively. He has worked at the university's Electrical Energy Laboratory. Since 1993, Dr. Bossche is a professor at the same university in the same field. His research is in the field of electrical drives, power electronics on various inverter types and passive components, and magnetic materials. He is also interested in renewable energy conversion. He is an author of the book entitled "Inductors and Transformers for Power Electronics". He was a starter of the spin-off companies Inverto n.v. (1990) and recently Alenco n.v. (2009). He is an IEEE member since 2000 and a senior member of IEEE since 2003.

Selim Koroglu received his M.Sc degree in Electrical and Electronics Engineering from Pamukkale University, Turkey in 2002 and his Ph.D. degree in Electrical Engineering from Yildiz Technical University, Turkey in 2010. Since 2011, Dr. Koroglu works as an assistant professor at Pamukkale University. His research interests include magnetic shielding, energy management, power systems, and power quality.

Selami Kesler received his B.Sc, M.Sc, and Ph.D degrees in Electrical Engineering from Karadeniz Technical University, Turkey in 1991, 1998, and 2006, respectively. He joined Karadeniz Technical University in 1992 and worked as a lecturer until 2004. He then joined the Department of Electrical Education, Pamukkale University, Denizli, Turkey, in 2004 as a lecturer. Since 2011, Dr. Kesler is an assistant professor at Pamukkale University. His fields of interest are power electronics, AC drives, dynamic analysis of the electrical machines, intelligent control techniques, and advanced DSPs.